We are IntechOpen, the world's leading publisher of Open Access books Built by scientists, for scientists

6,900
Open access books available

185,000
International authors and editors

200M
Downloads

Our authors are among the

154
Countries delivered to

TOP 1%
most cited scientists

12.2%
Contributors from top 500 universities

WEB OF SCIENCE™

Selection of our books indexed in the Book Citation Index
in Web of Science™ Core Collection (BKCI)

Interested in publishing with us?
Contact book.department@intechopen.com

Numbers displayed above are based on latest data collected.
For more information visit www.intechopen.com

Synergy between SMOS-MIRAS and Landsat-OLI/TIRS Data for Soil Moisture Mapping before, during, and after Flash-Flood Storm in Southwestern Morocco

Abderrazak Bannari, Hassan Rhinane and
Hicham Bahi

Additional information is available at the end of the chapter

Abstract

This chapter deals with soil moisture (SM) characterization over the Guelmim city and its neighborhood in the Southwestern Morocco that has been flooded several times over the past 50 years. To achieve this, space-borne SMOS and Landsat-8 OLI/TIRS data were preprocessed to correct several radiometric anomalies, and they were used. The SMOS brightness temperature data acquired before, during, and after the storm with 1-day temporal resolution and coarse spatial resolution (25 km) were transformed to the SM maps. OLI and TIRS data with moderate spatial and temporal resolutions were converted to Normalized Difference Vegetation Index (NDVI) and Land Surface Temperature (LST) to retrieve the Soil Moisture Index (SMI) maps. The results obtained were analyzed, intercompared, and validated against the compiled SM values from rainfall database (SM-RFE) delivered by NOAA climate prediction center Rainfall Estimator (RFE) for Africa. SMOS results show how the spatial variation of SM changes extremely at the regional scale before, during, and after the flash flood day-to-day. The SMI results converge toward the same conclusions showing a drastic SM change before and after flash flood highlighting the impact of inundation and the mud accumulation. By reference to the measured SM-RFE datasets, the validation of the derived SM maps exhibits a significant correlation ($R^2 \geq 0.89$). Globally, we observe a good complementarity among the considered data sources and processing methods for SM spatial information extraction, and the potential of their integration for the development of a prediction and monitoring model for flash flooding at the regional and local scales.

Keywords: soil moisture, SMOS, Landsat OLI/TIRS, land surface temperature, flash flood, storm, inundation, SMI

1. Introduction

Soil moisture (SM) affects the spatial variation of the biosphere and the atmosphere interactions through its influence on the balance of latent and sensible heat flux. It has been adopted by the *Global Climate Observing System* (GCOS) as an essential climate change variable and water resource management [1]. Its estimation and monitoring from space at the spatial and the temporal scales are useful information for hydrological, agricultural, and environmental applications, and modeling. It is required for drought and flood forecasting, natural disaster management, and assistance effort coordination during flooding periods. Moreover, it plays a fundamental role in the prediction of erosion and sediment loads in watershed streams according to topography and lithology [2–4]. In this context and in contrast with many conventional methods, remote sensing science and technology significantly contributed in the activities of SM estimation, flood damage assessment, and landscape management [5, 6]. Indeed, SM information can be derived from optical, thermal, passive, and active microwave remote sensing satellite sensors [2]. Optical sensors such as Landsat *Operational Land Imager* (OLI) exploring the *visible-near-infrared* (VNIR) and the *shortwave infrared* (SWIR) spectral domains characterize the SM based on the absorption feature, i.e., increased SM generally results in a decrease in reflectance. Moreover, the thermal infrared remote sensing, such as Landsat *Thermal Infrared Sensor* (TIRS), related the SM to the soil temperatures based on the heat and the thermal conductivity; thus, variation in SM is automatically related to the land surface temperature [6]. The intensity of passive microwave emission from moist soil is related to its dielectric constant; generally, the increase in SM leads to increase in microwave brightness temperature [7]. For active microwave, the magnitude of the retrodiffusion coefficient is related to the SM through the dielectric constants of soil and water [8]. Currently, *Synthetic Aperture Radar* (SAR) represents the best approach for obtaining spatially distributed surface SM at the medium local scale [2]. Nevertheless, developed by the ESA (*European Space Agency*) in collaboration with the *Centre National d'Études Spatiales* (CNES) in France, and the *Centro para el Desarrollo Tecnológico Industrial* (CDTI) in Spain, *Soil Moisture and Oceanic Salinity* (SMOS) was the first space-borne mission transporting onboard the *Microwave Imaging Radiometer using Aperture Synthesis* (MIRAS) instrument dedicated to near-surface (0–5 cm depth) SM mapping on a global scale using L-band. According to many studies, this band is one of the most promising approaches to monitor SM at the global scale with regular and high temporal resolution [7–9].

Furthermore, during the last four decades, the impact of climate change became an undeniable reality, with a broad consensus of the international scientific community on the significance of its impact on the environment and economic and social factors, especially in African countries. Morocco is a North-African country with a dominant (mostly) semiarid to arid climate and presents typical characteristics of Mediterranean landscapes vulnerable to land degradation processes, landslides, and desertification risks [10, 11]. Currently, Morocco is experiencing the longest dry episode of its contemporary history characterized by a reduction of precipitation and a rise in temperatures. In the southern regions of Morocco, the rainfall rarely occurs but with high intensity during a short period of time, which causes flooding problems and accelerated the erosion phenomenon and land degradation [3, 4]. According to Erskine and Saynor

[12], catastrophic floods are defined as events with a flood peak discharge at a rate of at least 10 times greater than the mean annual flood. Heavy rains often induce floods in Morocco, including flash floods, river floods, and mud floods during the rainy season. Indeed, in November 2014, violent storms caused flooding and impressive river floods in a large part of southern Morocco, especially in the city of Guelmim and regions, which are localized at the foot of the Atlas Mountains, with peaks rising to over 4000 m. According to SIGMA [19], this natural catastrophe caused the death of more than 46 persons and a significant damage to the infrastructure; villages were inundated causing thousands of houses to collapse, many oasis and agricultural fields were destructed, and power and telephone networks and several roads and bridges were damaged (**Figure 1**). Total losses were estimated about 0.6 billion US$ [13]. Consequently, the region of Guelmim was declared a "disaster area" by the Moroccan govern-ment. This area was not devastated for the first time; it has been flooded several times over the past 50 years, namely in 1968, 1985, 1989, 2002, 2010, and 2014. Unfortunately, in addition to the climate change impact, this situation happened because of the lack of emergency measures and a failure of development policy from the decision-makers. However, in order to improve the management of water regulation structures, to maximize water storage capacity, and to reduce the risks caused by floods, remote sensing (science and technology) has become a fundamental solution for flood monitoring and its impact assessment through SM [14]. The objective of this chapter is the SM mapping at the regional and local scales during the critical time of flash-flood storm exploring combined approaches based on SMOS-MIRAS and Landsat-8 (OLI and TIRS) datasets, respectively, and coarse and medium spatial resolutions.

Figure 1. Impressive flood and inundated village, destruction of road and bridge infrastructure, and driver rescues by helicopter (Guelmim region on 24 November 2014, photos from the web).

2. Material and method

The used methodology is summarized in **Figure 2**. It involves four fundamental steps: (i) data preprocessing, (ii) SM mapping from SMOS-MIRAS data, (iii) *Soil Moisture Index* (SMI) map retrieval from OLI and TIRS data, and (iv) obtained result analysis, interpretation, intercomparison, and validated against the compiled SM values from rainfall database (SM-RFE) delivered by NOAA climate prediction center *Rainfall Estimator* (RFE) for Africa.

2.1. Study site

Guelmim is a city in the south of Morocco (**Figure 3**) and is located at the foot of the western Anti-Atlas Mountains with peaks rising to over 2400 m above sea level (28° 59′ 02″ N, 10° 03′ 37″ W). It follows the course of underground shallow aquifers and dry rivers and it is characterized by a semiarid and arid subtropical climate. The temperature range varies from 12°C in January to 49°C in July. Annual rainfall averages between 70 and 120 mm/year. The geological formations that feed alluvium are granite, schist, quartzite, sandstone, limestone, dolomite, marl, conglomerate, andesite, and rhyolite. From a geological point of view, this region constitutes a complex synclinal, framed and surrounded in the N, W, and S by three Precambrian
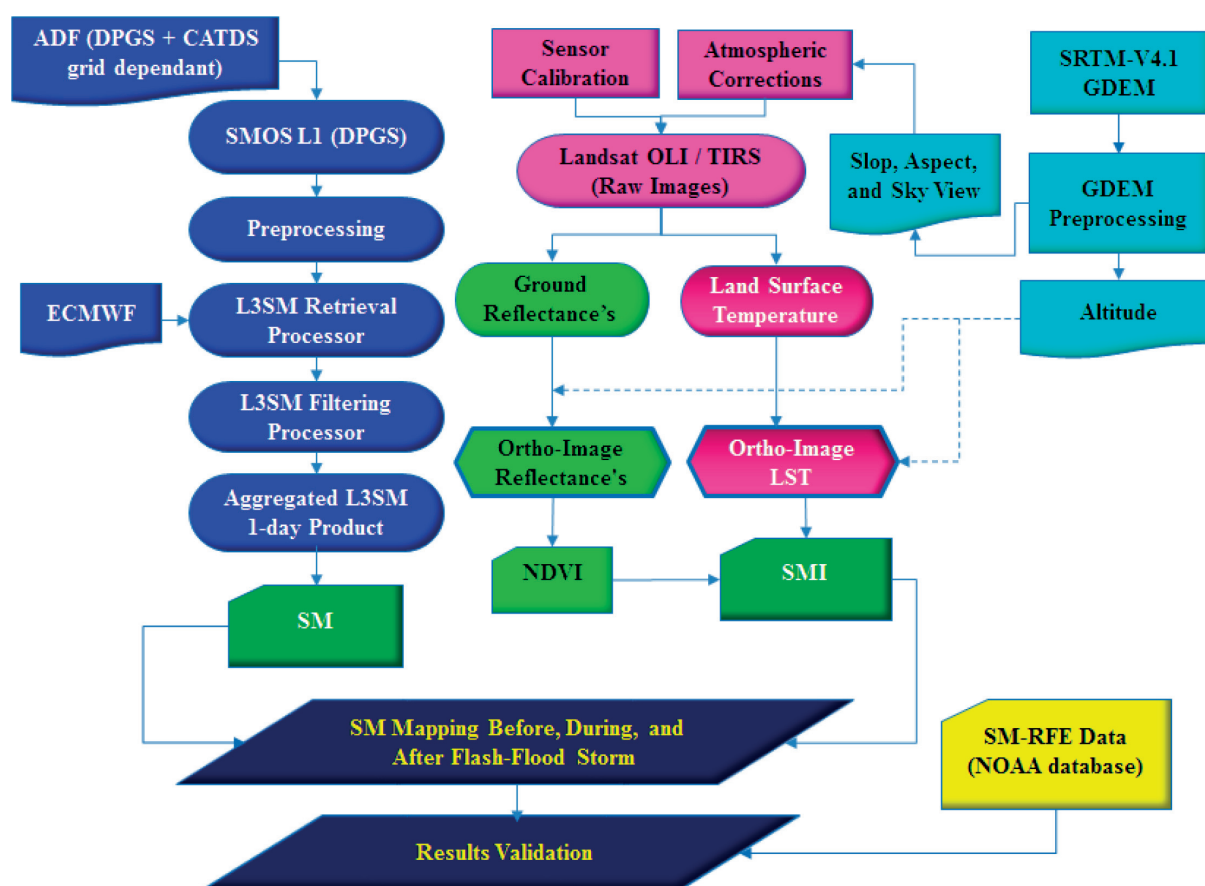
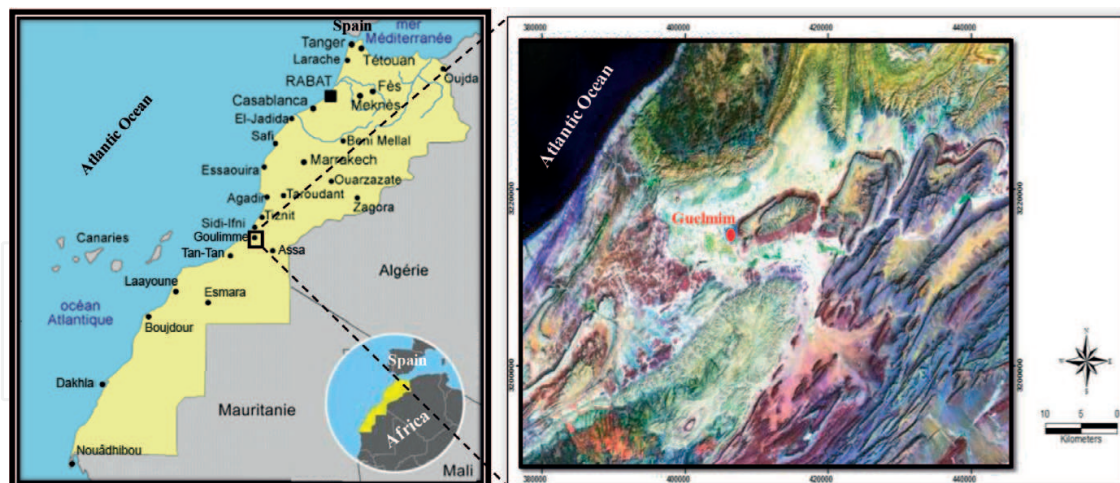

Figure 2. Methodology flowchart.

Figure 3. Study site.

anticlinal inlets [15]. The two main structural units in the region are the carbonate plateaus and the folded Bani Hills. The most important Infra-Cambrian and Cambrian carbonate plateaus are located in the north, consisting of a continuous area bordering from W to E the Ifni Inlet, Akhsass plateau, and the southern flank of the Kerdous inlet. The second one, located south, is formed by the external part of Jabal Guir-Taissa. These plateaus are surrounded by schist and sandstone formations of the Georgian age. At their foot begin large and elongated plains consisting of Acadian schist covered by Quaternary deposits. At the center of the Guelmim basin, Jabal Tayert is found, which is formed by green Upper Acadian schist and covered at the top by hard sandstone and quartzite bars. The Bani Jabal is a folded structure consisting of several aligned and NE-SW–oriented synclinals alternating with narrow anticlinals formed by Acadian or Ordovician sandstones and quartzites.

Furthermore, the Guelmim watershed covers a total area of approximately 7000 km^2, forming a network of wadis (rivers) along with several spreading floodwater areas (**Figure 4**). The hydrographic network is made up of three subwatersheds of the following main wadis: wadi Seyyad, wadi Noun, and wadi Oum Al-Achar. Wadi Seyyad originates at an altitude of 1200 m on the southern slopes of the Anti-Atlas Mountain. It flows in an E-W direction, composed of impermeable rocks and mainly receives numerous tributaries of its right bank; its watershed covers about an area of 2860 km^2. Wadi Noun drains the southern area, where the bit is marked with river beds that promote natural flooding. With a length of 143 km, its watershed comprises an area of about 2240 km^2. The wadi Assaka begins in the Akhsass massive at an altitude of 1150 m. It flows through the corridor between the Jebel Adrar and Guelmim west, discharging into the Atlantic Ocean. Finally, Wadi Oum Al-Achar, with a watershed of 1170 km^2, crosses a wide plain of 7 km and is located between the Tayert Hill and Ifni boutonnière. It drains the southern slopes of the Akhsass region, and its main tributaries are located in the plain. All three wadis lie on schistous impermeable large valleys, covered by low permeable Quaternary carbonates and fluviolacustrine silts. The confluence of the three wadis, downstream from Guelmim city, forms Wadi Assaka, which begins in the Akhsass massif at an altitude of 1150 m. It goes through the corridor between the Jabal Adrar and Guelmim west,
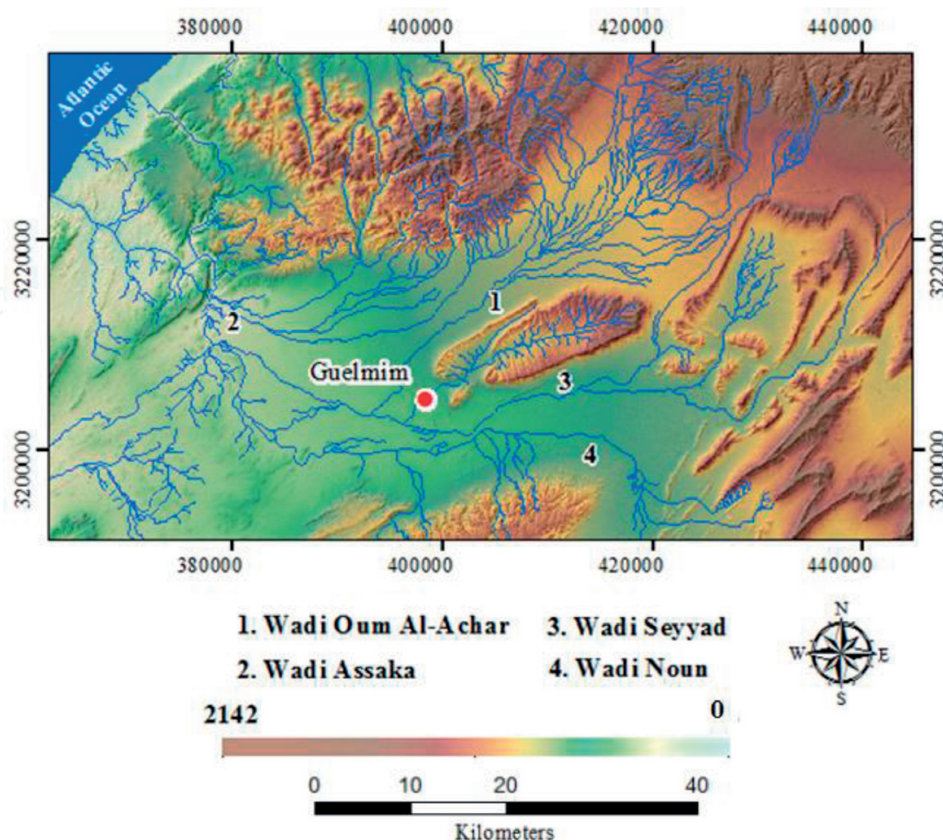
Figure 4. SRTM-V4.1 DEM with 30-m pixel size and the hydrological network overlaid on the study site.

eventually discharging into the Atlantic Ocean after crossing narrow gorges. This hydrographic system is often inactive, especially during the summer, when the flow is very low; however, it becomes active during the winter period (December to March).

2.2. SMOS data

SMOS is the first active remote sensing space-borne mission measuring the near-surface SM and sea surface salinity at the global scale [16]. Successfully launched on November 2, 2009, it is a small satellite-platform transporting onboard a 2D interferometer instrument named MIRAS composed of 69 small L-band receivers (21 cm and 1.4 GHz) measuring the phase difference of radiation in vertical and horizontal (V and H) polarizations under various incident angles with a high temporal resolution [16]. SMOS has a sun-synchronous orbit at 757 km altitude with a 06:00 Local Standard Time $\pm$ 15 min ascending equator crossing time. It provides global SM information with an accuracy better than 0.04 m^3/m^3 [17]. The pixel size of the acquired images is nominally 35 km at the scene center and resampled to 25 km. This information is used in predictive atmospheric, oceanographic, and hydrologic models to understand the climate system and the water cycle, to forecast the extreme natural events (floods and droughts), to manage the water resources adequately, and to improve the climate change impact assessment at the global and regional scales. In this study, the SMOS daily Level 1 (L1)

primary brightness temperature (BT) data acquired between November 1 and December 10, 2014, were preprocessed, processed, and downloaded using *Centre Aval de Traitement des Données SMOS*, http://www.catds.fr/Products/Available-products-from-CPDC (CATDS).

2.3. Landsat OLI/TIRS data

Since 1972, the Landsat scientific collaboration program between the NASA and USGS constitutes the continuous record of the Earth's surface reflectivity from space. Indeed, the Landsat satellite series support more than four decades of a global moderate resolution data collection, distribution, and archive of the Earth's continental surfaces to support research, applications, and climate change impact analysis at the global, the regional, and the local scales [18]. On February 11, 2013, the polar-orbiting Landsat-8 satellite was launched, transporting two push-broom instruments: OLI and TIRS. The OLI sensor collects land surface reflectivity in the VNIR and SWIR wavelength regions as well as a panchromatic band. The band passes are narrower in order to minimize atmospheric absorption features [19], especially the NIR spectral band (0.825 μm). Its design results in a more sensitive instrument with a significant amelioration of the *signal-to-noise ratio* (SNR) radiometric performance quantized over a 12-bit dynamic range (Level 1 data); raw data are delivered in 16 bit. This SNR performance and improved radiometric resolution provide a superior dynamic range and reduce saturation problems associated with globally maximizing the range of land surface spectral radiance and, consequently, enable better characterization of land-cover conditions. Furthermore, TIRS sensor incorporates two narrow thermal spectral bands (band 10:10.8 μm and band 11:12 μm) with a spatial resolution of 100 m, but resampled and delivered with 30 m to match OLI bands. These two bands use Quantum Well Infrared Photodetectors (QWIPs) to detect long wavelengths of light emitted by the Earth whose intensity depends on surface temperature. Moreover, they were designed to allow the use of "split-window" surface temperature retrieval algorithms, which allow the distinction between the temperature of the Earth's surface and that of the atmosphere [18]. Because of limited clear-sky conditions and cloud presence over the study site during the flash-flood storm that prevented the optical sensor observations, and the 16 days temporal resolution, only two pairs of raw images acquired by OLI and TIRS sensors were used in this research. The first pair (optic and thermic) was acquired on November 7, 2014, 2 weeks before the flash flood, and the second pair was collected on December 9, 2014, 8 days after the flash flood.

2.4. SRTM-V4.1 DEM data

The *Shuttle Radar Topography Mission* (SRTM) collected the most complete high-resolution digital topographic database over 80% of the Earth's land surface from 60° N to 56° S during an 11-day mission, which was flown aboard the space shuttle *Endeavor* from February 11–22, 2000 [20]. The fundamental objectives of this mission are to provide important information for NASA's Earth Sciences Enterprise, which is dedicated to understanding the total Earth system and the effects of human activity on the global environment [21]. Since 2000, the SRTM data have been provided in 30-m pixel size only within USA territory, while for the rest of the world, the data were available for public use at 90-m pixel size. In January 2015, the US

government released globally the full resolution of the original measurements (30-m pixel size). The data are projected in a geographic coordinate system using a WGS-84 geodetic reference and EGM-96 (*Earth Gravitational Model* 1996) vertical datum. According to USGS [21], at 90% confidence, the absolute vertical height accuracy is equal or less than ±16 m, there is a relative vertical height accuracy of less than ±10 m, and there is a circular absolute planimetric error of less than ±20 m and a circular relative planimetric error of less than ±15 m [20]. However, with reference to a topographic contours map (1:50,000), Bannari et al. [22] showed that the derived global height surface accuracy is ±3.15 m in Guelmim region. Moreover, they demonstrated that this accuracy is significantly influenced by topography; error is larger (±11.34 m) for high-altitude terrain with strong slopes, while it is smaller (±1.92 m) in the low-to-medium relief areas with indulgent slopes. This SRTM-V4.1 DEM was used for Landsat image preprocessing and for the study site topographic and hydrographic network characterization.

2.5. Soil moisture from rainfall estimator

Thanks to the close connection between rainfall and SM. Definitely, the ground rainfall measurement provides the accurate method to obtain information about daily rainfall, which is automatically used to estimate SM [23]. However, the spatially sparse network of meteorological stations and the temporally incomplete records at several stations across Africa leaves large parts of the continent unobserved. To resolve this problem, satellite-based algorithms have the advantage of providing full spatial coverage over Africa. The combination of the ground rainfall measurements and the daily satellite-based rainfall observations with contrasting estimation approaches are extremely valuable for rainfall monitoring and SM estimation over African territory. The RFE database setup by NOAA [24] is a product based on an algorithm exploiting four different data sources and several processing methods to estimate precipitation appropriately [24] in order to calculate after the standard water requirement satisfaction index to estimate soil moisture (SM-RFE) over Africa [25]. This independent SM-RFE database was used for the validation of the derived SM maps in this study.

2.6. Data preprocessing

2.6.1. SMOS

The SMOS data products are delivered in four levels. The L0 is the raw measured data with MIRAS radiometer and processed by the *Data Processing Ground Segment* (DPGS). The L1 is the primary BT data converted from the raw data (L0). The levels L2 and L3 products are, respectively, the retrieved SM and vegetation optical depth using an iterative scheme and multiangular BT observations [26]. The fundamental difference between these products (L2 and L3) is that the product L3 considers simultaneously several revisit observations over each pixel (multiorbit retrieval approach) to improve SM estimation [17]. These products are derived based on complex preprocessing chains at CATDS involving *Ancillary Data Files* (ADF), data obtained from SMOS combined with additional data from other sensors or models

for calibration (**Figure 2**). In this study, the daily SMOS L3 multiangular BT data products selected from CATDS data center were used to retrieve SM. The data were expressed at the top of the atmosphere (i.e., without correction for select reflected extraterrestrial sky and atmosphere contributions) and at predefined incident angles varying from 2.5 to 62.5° with 5° steps. They were delivered for both ascending and descending orbits, and projected on a global EASE grid with 25 km pixel size. The preprocessing steps consist of the following operations: spatial resolution filtering, *Radio Frequency Interference* (RFI) detection (to exclude data with a probability of RFI larger than 0.2, and urban or water cover fractions larger than 0.1), correction of grid nodes where sun specular effect occurs, computation of radiometric noise correction factor, computation of the initial validation index, and computation of atmospheric and sky contribution [27]. The reader can find more details about the preprocessing steps in Kerr et al. [17].

2.6.2. Landsat OLI/TIRS

Optical sensor calibration and atmospheric corrections are fundamental preprocessing operations to restore the images' radiometric quality. The changes caused by these artifacts can be mistakenly attributed to changes in the land use and ground biophysical components, and errors can propagate in all subsequent image processing steps, such as spectral indices calculations, multitemporal analysis, climate change modeling, etc. [28, 29]. The *Canadian Modified Simulation of a Satellite Signal in the Solar Spectrum* (CAM5S) based on the Herman radiative transfer code [30] was used for atmospheric parameter simulation in OLI spectral bands to calculate all the requested atmospheric correction parameters. To preserve the radiometric integrity of the images, absolute radiometric calibration and atmospheric effects were combined and corrected in one step. Likewise, to eliminate the distortions caused by the relief and the shadow impact, especially in the Guelmim study area with Atlas Mountains peaks of more than 2400 m, an orthorectification was conducted using SRTM-V4.1 GDEM [22]. In addition, topographic attributes such as altitude, slope, aspect, and sky view, integrated into the orthorectification approach, were extracted from this DEM [31]. The Rational-Function Model implemented in the Ortho-Engine module of PCI-Geomatica was used in this step that allows the corrections of the parallax effect at the spatial arrangement of pixels along track, disruptive effects caused by shadow and topographic variability, as well as the residual atmospheric artifacts caused by altitude variability (**Figure 2**). To preserve the image radiometric integrity, geometric corrections have been combined into a single step with the correction of topographic effects [29]. Furthermore, the preprocessing of TIRS data (band 10) was done by conversion of the digital numbers to BT using the Planck radiance function (Eq. (1)) and the thermal calibration constants (K_1 and K_2) provided in the images' metadata files [32]. Then, the BT was transformed to *Land Surface Temperature* (LST), which is a key variable in Earth environment research for calculating the *Soil Moisture Index* (SMI). The LST was calculated based on a method that combines the vegetation cover fraction (P_v) derived from the NDVI and the emissivity (ε), expressed by the Eq. (2) [33]. Based on the NDVI histogram thresholds (Eq. (4)), the vegetation fraction (P_v, Eq. (5)) was estimated from $NDVI_{min}$ and $NDVI_{max}$ referring, respectively, to nonvegetated and very dense vegetated land covers.

$$T_b = \frac{K_2}{\ln\left(\frac{K_1}{L_\lambda} + 1\right)} \tag{1}$$

$$LST = \frac{T_b}{[1 + (\lambda \times T_b/C_2) \times \ln(\varepsilon)]} \tag{2}$$

$$C2 = h \times c/s \tag{3}$$

$$\varepsilon = \begin{cases} a + b\,\rho red & \text{when NDVI} < 0.2 \\ \varepsilon_v P_v + \varepsilon_s(1 - P_v) + d\varepsilon & \text{when } 0.2\ \text{NDVI}\ 0.5 \\ \varepsilon_v + d\varepsilon & \text{when NDVI} > 0.5 \end{cases} \tag{4}$$

$$P_v = \left[\frac{\text{NDVI} - \text{NDVI}_{min}}{\text{NDVI}_{max} - \text{NDVI}_{min}}\right]^2 \tag{5}$$

$$\text{NDVI} = (\rho_{nir} - \rho_{red})/\rho_{nir} + \rho_{red}) \tag{6}$$

where T_b is at-satellite BT, λ is the wavelength of emitted radiance, and K_1 (774.89) and K_2 (1321.08) are the calibration constants for the band 10. $C_2 = 1.4388*10^{-2}$ m K and it is presented by Eq. (3). ε is the emissivity computed from Eq. (4) [33]. h is Planck's constant = $6.626*10^{-34}$ J/s, c is the velocity of light = $2.998*10^8$ m/s, and s is Boltzmann constant = $1.38*10^{-23}$ J/K. ε_v is the vegetation canopy emissivity, ε_s is the bare soil emissivity, and $d\varepsilon$ is the internal reflection emissivity due to cavity effect, while ρ_{red} and ρ_{nir} are the surface reflectance in the red (OLI-4) and near-infrared (OLI-5) spectral bands, respectively.

2.7. Data processing

2.7.1. SMOS

The multiangular BT data products were processed using the SMOS retrieval algorithm to derive SM. Based on the *L-band Microwave Emission of Biosphere* (L-MEB) radiative transfer model [16], this algorithm considers an iterative approach minimizing the difference between the observed and estimated BT at H and V polarizations, for a variety of incident angles. Moreover, it includes a number of parameterizations to capture effects of vegetation structure and soil roughness on polarization and angular properties of BT emitted from land surfaces [34]. This algorithm has been calibrated and validated several times using *in situ* measurements [26, 35], and recent validation process shows an accuracy around 0.04 m³/m³ in comparisons with observations from watershed networks [36]. The soil temperature product derived from the *European Centre for Medium-Range Weather Forecasts* (ECMWF) was introduced in this algorithm to provide a ground reference "calibration-information" useful for the time series analysis to retrieve the most accurate possible SM maps [36]. A multilinear regression approach was achieved over the considered data using calibrating coefficients and several ancillary data extracted from ADF until the algorithm finds the best set of parameters to derive the daily L3 SM maps. More details about the processing process are described in Kerr et al. [17].

2.7.2. OLI and TIRS

SM conditions at different times (i.e., between droughts and flood periods) can change extremely. In the literature, we know that the SM in the first centimeters of the soil surface is strongly related to the emitted BT measured with L-band [37]. Moreover, as mentioned before, other studies have shown the potential of the combination of LST derived from thermal infrared radiation and NDVI to estimate and to monitor SM conditions. The idea behind this combination is the linkage between hydrological cycle (water content in soil) and biophysical parameters (vegetation cover density), and the connection in turn interacts with atmosphere-biosphere coupled system. Exploring this concept, an empirical parametrization was established between LST and NDVI (scatter-plot in 2D space) by Zeng et al. [38] who showed how land surface biophysical properties vary as a function of SM conditions. Then, they proposed the SMI, whose values are ranged from 0 to 1 indicating, respectively, severe drought and very moist conditions. This SMI is defined as follow [38]:

$$SMI = \frac{LST_{max} - LST}{LST_{max} - LST_{min}} \tag{7}$$

$$LST_{max} = a_1.NDVI + b_1 \tag{8}$$

$$LST_{min} = a_2.NDVI + b_2 \tag{9}$$

where LST_{max} and LST_{min} are the maximum and minimum of land surface temperatures for a given NDVI. LST is the observed land surface temperature at the given pixel for a given NDVI. a_i and b_i (i = 1, 2) are parameters obtained by the linear regression (a is the slope and b is the intercept) defining both dry and moist edges of the data.

3. Results analysis and discussion

3.1. Topographic and hydrographic network analysis

The topography controls the flow and speed of water, as well as the direction of its dispersion during the inundation. To understand the SM and the flash-flooding mechanisms in the study area, it is so important to analyze the geomorphologic and the topographic variations, and the hydrographic network, and their contribution in these natural hazards. The study site has two main geomorphologic units, the limestone plateau of the Anti-Atlas and quartzite ridges, which is limited by the Atlas Mountains (in the N, S, E, and W) as a natural barrier, which leads to water retention in case of high precipitation intensity. It is characterized by broader valleys and depressions surrounded by hills with heights varying from 153 to 2060 m (**Figure 4**) and steep slopes varying between 9.5 and 26°, which converge toward the interior of the Guelmim plain. The topography of this plain is classified into seven classes whose altitude range vary significantly between 200.0 and 573.5 m, starting from northeast to southwest with approximately 373.5 m height difference. This morphology leads to water retention in the case of rainstorm and, consequently, contributes to the risk of inundation. Thus, it is one of the

factors supporting the risk of flash floods. Indeed, as illustrated in **Figure 4**, the hydrographic network is made up of three subwatersheds and four main wadis (wadi Seyyad, wadi Noun, wadi Assaka, and wadi Oum Al-Achar) that flow on a steep slope. It can be seen that the slope orientation and direction of the Guelmim watershed are facing the center of the plain. Moreover, a hill in the East forms a natural barrier with a denivelation of approximately 100 m, which creates a natural basin promoting the accumulation of water and sediments over approximately 14 km distance. The topography variation starting from the foot of Guelmim city (NE-SW) illustrates a very strong slope (26°), which ends on a terrain with concave morphology forming a natural basin. This basin facilitates the accumulation of storm flood, thereby concentrating runoff water, sediment, and mud load. The highest altitude values (between 500 and 2400 m) with the steep slopes and ridges (corresponding to schist and soft Quaternary deposits), representing the streams and drainage system, depressions, and broader-valleys, are related to a relatively high slope gradient ≥20°. They contribute significantly to the erosion's aggressiveness associated with a significant degree of sediment transportation and land degradation risk process. Hard rocks, such as Precambrian quartzite, Adoudounian limestone and dolomite, Ordovician quartzite and sandstone, and Georgian black limestone, characterize these zones. The lowest altitude values represent relatively flat areas with a low slope (≤4°) in the NE-SW direction, which is the hydrographic network direction. In addition, morphological factors influence the susceptibility to flooding and sediment deposition and accumulation, because water tends to flow and accumulate in response to gradients in gravitational potential energy. In general, this first analysis demonstrates clearly that rainfall and topography are the major contributing factors to flash flooding and catastrophic inundation in the study area. The runoff waterpower delivers vulnerable topsoil and contributes strongly to the erosion and land-degradation process after a flood storm in the Guelmim basin. It then transports soil material and sediments to the plain through natural action, i.e., water power and gravity. As illustrated by the photos in **Figure 1** that were acquired during the same day of the flood storm, the water color was dark-red because of its turbidity as it was very rich with sediments and eroded particles. Certainly, the role of the lithology associated with the terrain morphology is decisive in the erosion risk, land degradation, and spatial repartition of SM in this region. This analysis shows how the topographic and hydrographic networks contribute to inundations in the study site and, therefore, highlight the areas subject to different moisture levels.

3.2. SMOS result analysis

As discussed before, using the daily SMOS L3 data, SM maps were generated for each day from the 1st of November to the 10th of December over the Moroccan territory. During these 40 days, **Figure 5** illustrates the SM temporal variation over the Guelmim city and region day-by-day before, during, and after the flood storm. These SM values are the average of four SMOS pixels (2 by 2) covering the study site, which is approximately 50 by 50 km^2. Increased SM values are observed from 2% (1st of November) to 22% (4th of November) during the dry period and after the first precipitations, respectively. Then, the moisture values gradually decreased in the soil from 22 to 4%, respectively, between the 4th and 19th of November. A strong increase of SM took place between the 19th and 21st of November reflecting events with
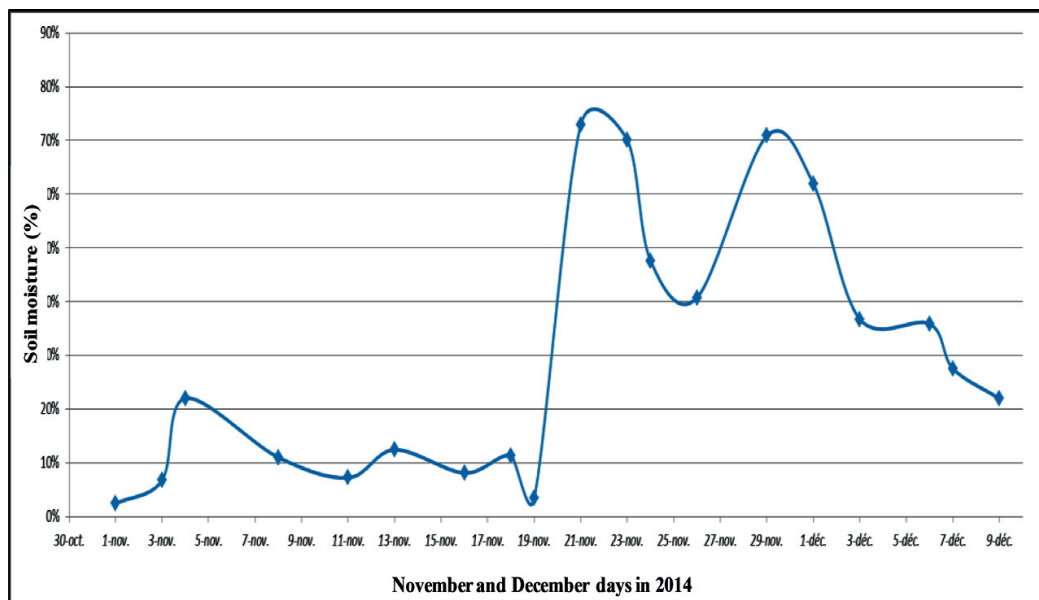
Figure 5. Soil moisture variability over Guelmim region between the 1st of November and the 9th of December 2014 using SMOS satellite data.

a flood peak discharge. It can also be observed that the peaks marked these dates are followed with succession periods of rain maintaining high SM conditions. In fact, during 1 week (19th to 26th of November), SM values remain above 40% with a high peak (SM of 72%) on the 22nd of November. Then, a new flood peak discharge was registered (SM of 74%) on the 29th of November, and progressively the SM values decreased to 23% on the 9th of December. Globally, the highest values (SM > 40%) were recorded between 21st of November and 03rd of December, period when the floods were at their peak. In the following analysis, only six SMOS SM maps reflecting six decisive temporal periods have been chosen to express changes of SM values during these flood events. **Figure 6a** illustrates the SM map for the 2nd of November expressing a severe drought situation over the Moroccan territory, especially over Guelmim region with 2% water content in the soil. On the 07th of November (acquisition date of the first Landsat OLI/TIRS image before the flash flood), the SM value gradually increased to 13% in the southwestern Morocco, but in the center and north regions, the storm had already begun and SM values were, respectively, around 35 and 60%. **Figure 6c** and **d** illustrates the SM maps during the extreme flood events over the majority of the southern Moroccan territory, including Guelmim city and neighborhood; recorded SM values were 73% and 43% for November 21 and 27, 2014, respectively. As a consequence of high precipitation causing very destructible floods, strong changes of SM were also observed on the 1st of December recording 65% water content in the soil (**Figure 6e**). Then, on the 9th of December that coincides with the acquisition date of the second Landsat OLI/TIRS image (8 days after the flash flood), **Figure 6f** shows a decrease in precipitation and the recorded SM content was around 22%. With reference to the calculated SM from SM-RFE NOAA database, the validation of these SMOS SM maps exhibit a significant correlation ($R^2 > 0.90$) at $p < 0.05$ using a first-order polynomial function. This meaning is in agreement with several other results of SMOS validation around the world [36, 39, 40].
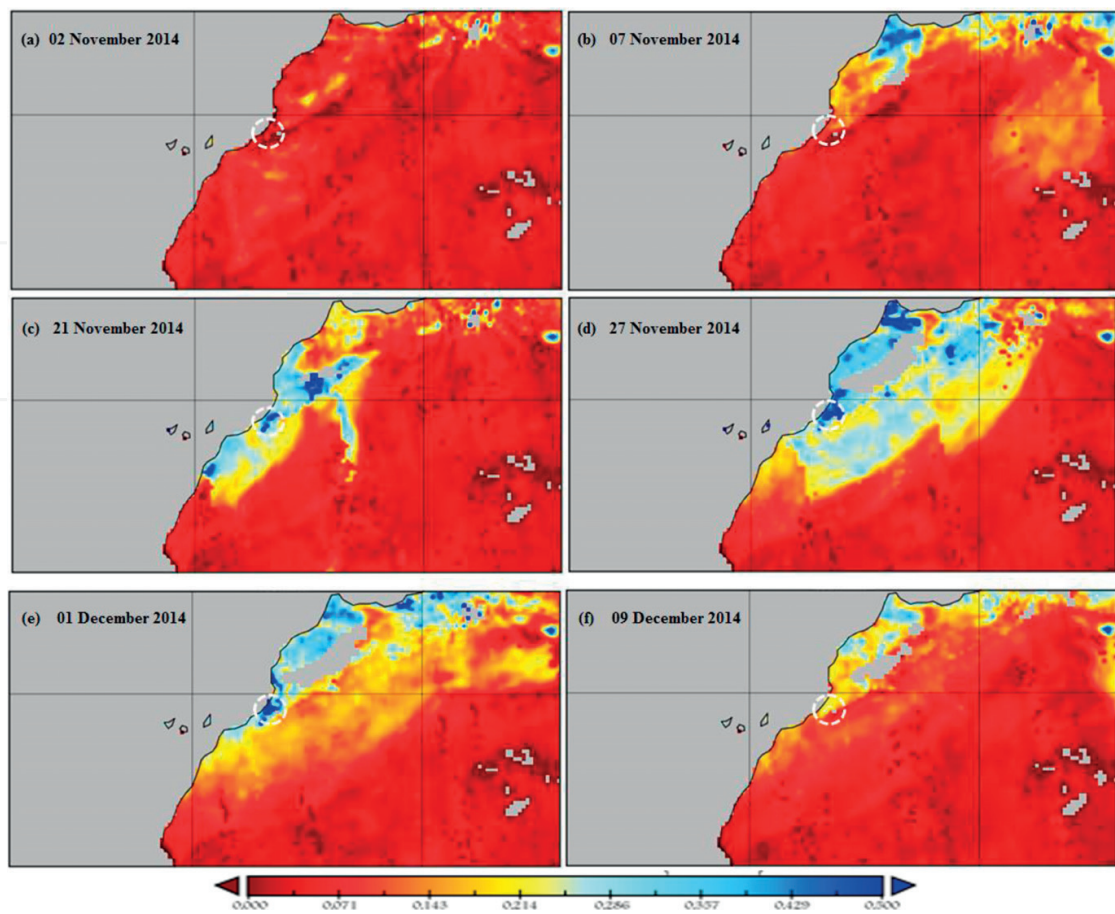
Figure 6. SM maps derived from SMOS data over Morocco (Guelmim region surrounded by the white circle) for November 2, 7, 21, and 27, 2014, as well as for December 1 and 9, 2014.

Furthermore, we observe generally that these derived SMOS maps allow SM characterization and monitoring with excellent temporal resolution over a very large territory or at a country scale, independently to the meteorological conditions. It is possible to predict day-by-day the power, the cycle, and the direction of the storm progress. Obviously, the information is very useful for a warning system development for flash-flooding prediction. Nevertheless, despite these significant and positive potentials, unfortunately, the major disadvantage of SMOS data for this type of application is the coarse spatial resolution that is not sufficient for detailed and accurate information extraction at the locale medium or large scales. For instance, for rescue organization, the roads and river networks are not visible on this kind of data. Moreover, it is impossible to predict the river dynamics and their relation with topographic attributes for relevant risk management in order to organize evacuations of the population and vehicles to the less hazardous spots. Globally, this type of data does not allow us to understand and to study what it is missing in the field (real world) to ensure the safety of population. Moreover, according to high spatial distribution and heterogeneity of SM, there is a need to characterize it at relevant spatial scale to improve the representation of runoff and precipitation in hydrologic and weather prediction models, resulting in improved predictive skills (drought, flood, etc.). Also, the challenge will be mainly to characterize complex mixed pixels including a variety of targets: water, crops, fallow layer, urban, roads, etc. Indeed, the SMOS-MIRAS sensor observes

a very large watershed as a whole target in one pixel, and the Guelmim city and regions are covered by 4 pixels that are considering the city as a bare soil. In addition to the pixel complexity, in this mountainous area, SMOS pixels present a mixture of different topographic facets with varying slopes and azimuths, shadowing and adjacency effects, inducing effects which may eventually render the SM estimation less accurate. Indeed, in areas with strong topography such as the Moroccan Atlas Mountains, we know that SM is controlled automatically by gravity-driven water to horizontal regions or areas with very low topographic variation. In such case, SM can be related to topographic features through catchment hydrologic models that require a medium spatial resolution. While, in flat areas, soil mineralogy composition and texture and vegetation cover properties have a stronger impact than topography. Obviously, for addressing the monitoring of SM for flash-flood storm and hydrological applications in areas with high altitude variations and complicated soil mixt-pixels, medium spatial resolution is required. This conclusion is corroborated by several other studies about flood modeling [41], hydrological model calibration [42], and flood simulation [43]. Other studies have revealed that the contribution of satellite remote sensing for SM for runoff modeling is still imprecise [44]; others obtained moderate improvement in hydrological modeling through the assimilation of SM derived from satellite data [45], while others obtained insignificant performances [46]. These distinct results have to be attributed to the inherent uncertainties and issues involved in the use of satellite with coarse spatial resolution for SM estimation and its integration in flood prediction and hydrological modeling. However, other optimistic studies summarize the emerging SM applications, the open issues, and the future opportunities given by new generation of satellites planned for near future [47]. Of course, we share this optimism because, for instance, the synergy between the SMOS coarse spatial resolution and medium spatial resolution of optical and thermal data is likely helpful to achieve a multiresolution SM retrieval approach. Several downscaling methods and integration with medium or low resolutions data such as Landsat-8 or MODIS, as well as using other ancillary data, are required to quantify subpixel heterogeneity of SM. Certainly, the combination and integration in GIS environment of SM subpixel values with the density of the hydrographic and road networks, as well as topographic features (as discussed above), will contribute significantly to inundation monitoring and management.

3.3. MSI result analysis

Figure 7 illustrates the geographic location and density of vegetation cover mapped with NDVI before the flood storm. As a consequence of climate change impact and deforestation in the region, scattered vegetation cover (in green color) is observed in the middle of the Guelmim plateau and along the river beds, represented by small agricultural fields and oases with palm trees. At the top of the mountain (N-W and N-E), a relative high grass and shrub density can be observed, because this high-altitude region benefits from a mild oceanic climate (near to the coast) and the dew, which irrigate significantly this vegetation. Contrariwise, in the south, southeast, and southwest, the vegetal cover is completely absent. Despite the fact that a vegetation index alone is not generally helpful for flood impact assessment or sediment accumulation estimation, the NDVI before and after the flood storm was calculated and integrated with LST for the SMI map derivation. Only the NDVI before flooding is presented
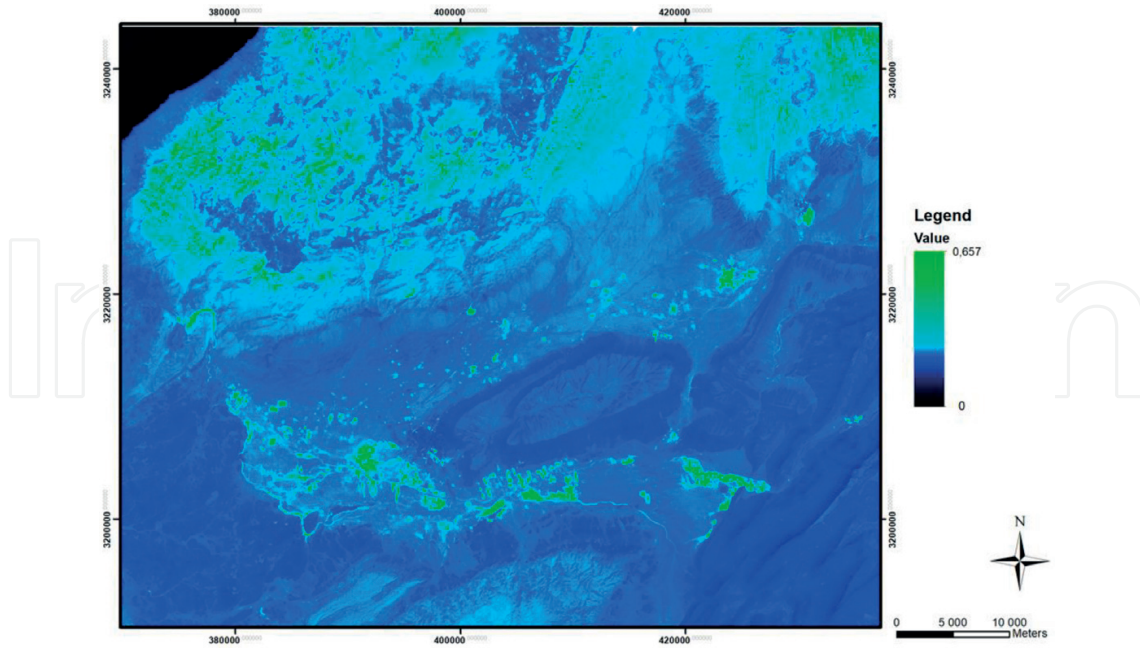
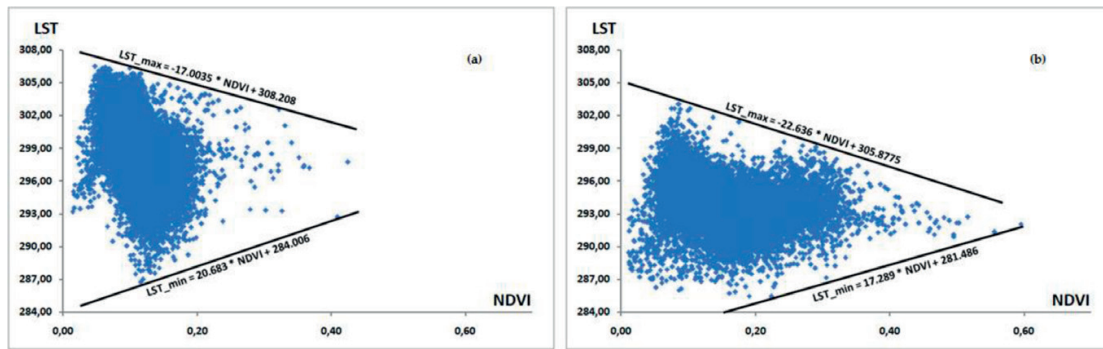**Figure 7.** NDVI before the flood storm.

Figure 8. A scatter plot between LST and NDVI before (a) and after (b) the flood storm.

here; after flooding, it showed similar patterns except a very modest increase of herbaceous vegetation density in high-altitude areas. Furthermore, SMI maps show their usefulness in this study before and after the flood storm and we will discuss them thereafter.

Exploiting the scatter plots between LST and NDVI, before (**Figure 8a**) and after (**Figure 8b**) the flood, the necessary coefficients (*a1*, *a2*, *b1*, and *b2*) for SMI (Eq. (7)) were obtained using linear regression for both dry and wet edges (Eqs. (8) and (9)). Then, the final SMI equations were established and implemented using OLI and TIRS data acquired before and after flood storm (SMI-1, Eq. (10)) and (SMI-2, Eq. (11)).

$$SMI\_1 = \frac{-17.00 \ NDVI + 308.21 \ - \ LST}{-37.68 \ NDVI \ + 23.72} \tag{10}$$

$$SMI\_2 = \frac{-22.64.\text{NDVI} + 305.88 \quad - \quad \text{LST}}{-39.93.\text{NDVI} \; + 24.39} \tag{11}$$

Figure 9 illustrates the SMI map before the flash flood, named SMI-1, highlighting the water content variability over the study site in different classes. High SM (> 60%) value classes are observed in areas located at the top of the mountains, surrounding Guelmim city, where vegetation cover is relatively dense. Also, significant SM content (∼35%) characterizes small agricultural fields and oases with scattered vegetation cover, hydrographic network, watershed, and ravines. In the Guelmim plain, SMI values are very low and close to 0. In general, these lower SMI values indicated heavier drought occurrence, which is coherent with SMOS SM values over the study site during the same day. Furthermore, we observe that SMI-1 based on LST is sensitive to rock thermal properties, soil surface composition (roughness and mineralogy), soil hydraulic properties (unseen water, capillarity, and evaporation) that typically occur in the subsurface, topographic variation, and steady state groundwater temperature with a spatially homogeneous temperature distribution. Therefore, these sensitivity variations highlight the SM as a function of the geomorphology and the topography on the terrain. Statistical fit between several homologous points extracted from SMI-1 and the SM-RFE database shows significant correlation (R^2 of 0.90). Furthermore, **Figure 10** illustrates the derived SMI map, named SMI-2, from the OLI/TIRS data acquired on the 9th of December, i.e., after several days of flooding that occurred between November 21st and December 1st. It describes different SM classes following the subwatersheds, topographic variations, rock properties, and soil composition. Highest SM values (>75%) are detected in high altitude (read color class) associated with dense vegetation cover. However, in the south and southeast without vegetation cover, the high SM values are related to the rock types forming
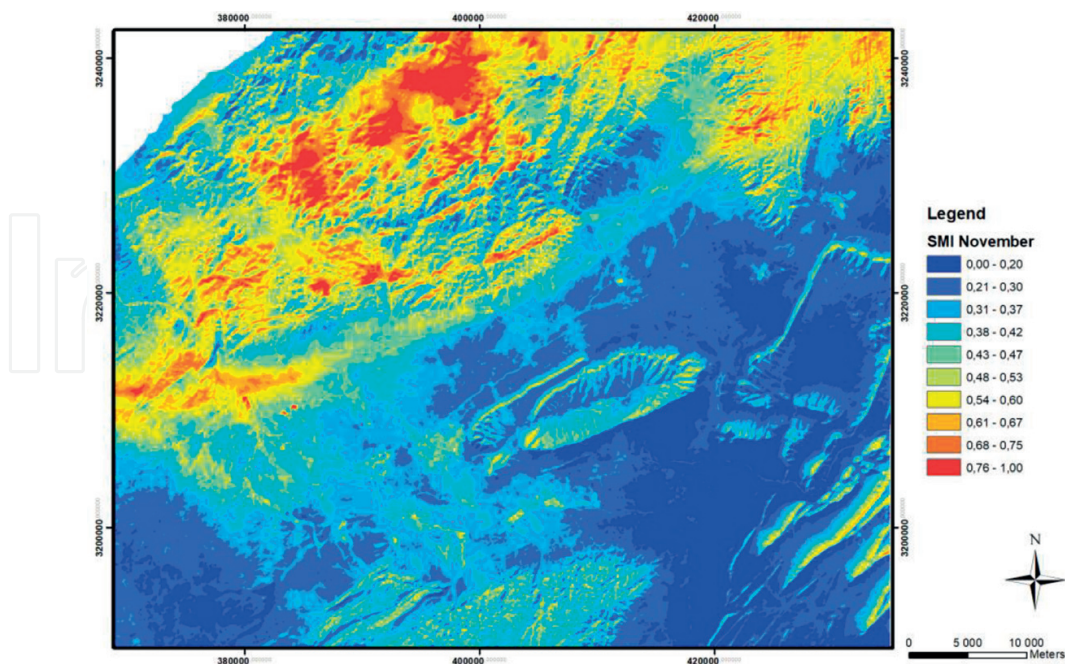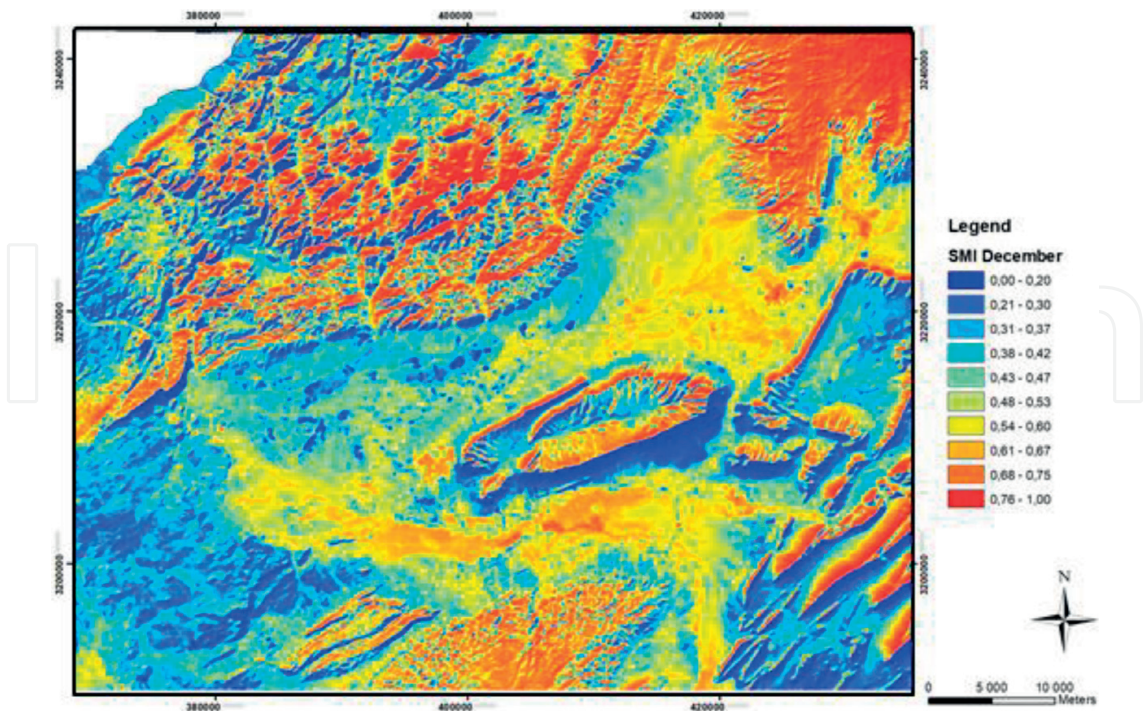

Figure 9. SMI-1 before the flood storm.

Figure 10. SMI-2 after the flood storm.

a synclinal located at high altitudes. In areas where water flow coming from the mountains following narrow streams via dejection cones, as well as the wadis (rivers) and their tributaries, was drained by gravity toward the plain of Guelmim where water and mud are accumulated forming a vast pool (E-W direction), the calculated SM values are very significant (45% ≤ SM ≤ 70%), i.e., green, yellow, and brown color classes. Areas of this class are covered by low permeable Quaternary carbonates and fluviolacustrine silts, allowing the water retention. Finally, the areas with relative medium slopes (9.0° to 20°) exhibit SM values between 30% and 42% (blue-cyan color class), while low SM values (<10%) are identified in areas with steep slopes facilitating water transition (blue color class). These highest SM values detected by SMI-2, 15 days after the flood storm, testify the strength of this tempest that killed 46 people and severely damaged the region's infrastructure (**Figure 1**). These results are in agreement with those retrieved from SMOS, and its validation against SM-RFE database also shows a significant correlation (R^2 of 0.95).

4. Conclusions

Flood-storm forecasting requires data collection, preprocessing, processing, and derived product interpretation to estimate the amount of runoff that will occur spatially and temporally. Then, the forecaster can identify when and where problems could occur for natural disaster management, and people assistance effort coordination during flooding periods. Among others, monitoring SM is a fundamental key for decision makers to predict and to manage flood event before, during, and after flash-flood storm. To meet these concerns, the past

10 years have witnessed the emergence of potentially transformative new remote sensing technologies and methods for SM estimation, which are beginning to fundamentally alter the possibilities for water-cycle and flood risk monitoring at different scales. The aim of this chapter is SM characterization over the Guelmim city and its neighborhood in the Southwestern Morocco that has been flooded several times. To achieve these, space-borne SMOS and Landsat-8 OLI/TIRS data were used. The SMOS BT data acquired before, during, and after the storm with 1-day temporal resolution and coarse spatial resolution (25 km) were preprocessed, processed, and transformed to the SM maps. OLI and TIRS data acquired 2 weeks before and 2 weeks after flood storm were preprocessed and transformed to NDVI and LST, and then combined to retrieve the SMI maps. The results obtained were analyzed and validated against the compiled SM values from rainfall data (SM-RFE) delivered by NOAA climate prediction center RFE for Africa.

SMOS results show how the spatial variation of SM changes extremely before, during, and after the flash flood with excellent temporal resolution over a very large territory (or at a country scale) independently to the meteorological conditions. It is possible to predict day-by-day the power, the cycle, and the direction of the storm progress. Obviously, this information is very useful for a warning system development for flash-flood prediction. By reference to the measured SM-RFE database considered as a ground truth, the validation of the derived SMOS SM maps exhibit a significant correlation ($R^2 > 0.90$). However, despite these significant and positive potentials, the major disadvantage of SMOS data for several hydrological applications, especially flash-flood storm monitoring, is unfortunately the coarse spatial resolution that is not sufficient for detailed and accurate information extraction locally or regionally at the large or medium scales. Furthermore, although the SM maps have been derived from OLI and TIRS based on different wavelengths, unlike acquisition modes, and using different image-processing methods, the results converge toward the same conclusions. The MSI results show a drastic SM change before and after flash flood, highlighting with more details the impact of inundation and the mud accumulation in the study site. Based on NDVI and LST, the SMI-1 shows certain sensitivity to the soil and rock thermal properties, the soil surface composition, the soil hydraulic properties, etc. Moreover, these variations highlight the SM as a function of the geomorphology and the topography on the terrain. For validation purposes, statistical fit between several homologous points extracted from SMI-1 and SM-RFE database shows a significant correlation (R^2 of 0.90). Likewise, 15 days after the flood storm with a saturated soil moisture, SMI-2 describes SM correctly. Indeed, significant correlation was obtained (R^2 of 0.95) when validating the derived SMI-2 map against SM-RFE datasets.

In this chapter, although the SM maps have been derived from data acquired with different sensors and using different image-processing methods, the results converge toward the same conclusions, before and after the flood storm. However, even if the spatial resolution of SMOS observations is adequate for several global applications, it is restricted to regional and local studies for flash-flood storm monitoring that requires medium spatial resolution. On the other hand, despite the potential of Landsat-8 (OLI and TIRS) medium scale data, they remain sensitive to other environmental factors especially meteorological conditions, which make the SM retrieval impractical during the storm. Nevertheless, the synergy between coarse spatial resolution microwave data and medium resolution optical-thermal data is likely helpful to

achieve a multiresolution SM retrieval approach as previously discussed. Their integration in a GIS environment with other ancillary data will contribute significantly in the development of a prediction and monitoring model for flash flooding at the regional and local scales.

Acknowledgements

Author details

Abderrazak Bannari[1]*, Hassan Rhinane[2] and Hicham Bahi[3]

*Address all correspondence to: abannari@agu.edu.bh

1 Department of Geoinformatics, College of Graduate Studies, Arabian Gulf University, Manama, Kingdom of Bahrain

2 Department of Geology, Faculty of Sciences Ain Chock, University Hassan II, Casablanca, Morocco

3 Department of Computer Sciences, Faculty of Sciences Ain Chock, University Hassan II, Casablanca, Morocco

References

[1] IGWCO. Integrated Global Water Cycle Observation: Community of Practice. Earth Observation Group [Internet]. 2010. 20 p. Available from: http://www.wmo.int/pages/prog/hwrp/chy/chy14/documents/ms/IGWCO.pdf [Accessed: Jan 10, 2018]

[2] Moran MS, Peters-Lidard CD, Watts JM, McElroy S. Estimating soil moisture at the watershed scale with satellite-based radar and land surface models. Canadian Journal of Remote Sensing. 2004;**30**(5):805-826. DOI: 10.5589/m04-043

[3] Bannari A, Ghadeer A, El-Battay A, Hameid NA, Rouai M. Assessment of land erosion and sediment accumulation caused by runoff after a flash-flooding storm using topographic profiles and spectral indices. Advances in Remote Sensing. 2016;**5**:315-354. DOI: 10.4236/ars.2016.54024

[4] Bannari A, Kadhem G, El-Battay A, Hameed NA, Rouai M. Detection of areas associated with flash floods and erosion caused by rainfall storm using topographic attributes, hydrologic indices, and GIS. In: Pirasteh S, Li J, editors. Global Changes and Natural Disaster Management: Geo-Information Technologies. Springer International Publishing: Germany; 2017. pp. 155-174. DOI: 10.1007/978-3-319-51844-2.chp.13

[5] Joyce K, Belliss S, Samsonov S, McNeill S, Glassey P. A review of the status of satellite remote sensing and image processing techniques for mapping natural hazards and disasters. Progress in Physical Geography. 2009;**33**:183-207. DOI: 10.1177/0309133309339563

[6] Friedl MA, Davis FW. Sources of variation in radiometric surface temperature over a tallgrass prairie. Remote Sensing of Environment. 1994;**48**(1):1-17. DOI: 10.1016/0034-4257(94)90109-0

[7] Njoku E, Jackson E, Lakshmi V, Chan T, Nghiem S. Soil moisture retrieval from AMSR-E. IEEE Transactions on Geoscience and Remote Sensing. 2003;**41**:215-229. DOI: 10.1109/TGRS.2002.808243

[8] Ulaby FT, Dubois PC, Van Zyl J. Radar mapping of surface soil moisture. Journal of Hydrology. 1996;**184**:57-84. DOI: 10.1016/0022-1694(95)02968-0

[9] Kerr YH, Waldteufel P, Wigneron JP, Martinuzzi JM, Font J, Berger M. Soil moisture retrieval from space: The soil moisture and ocean salinity (SMOS) mission. IEEE Transactions on Geoscience and Remote Sensing. 2001;**39**(8):1729-1735. DOI: 10.1109/36.942551

[10] Bannari A, El-Harti A, Haboudane D, Bachaoui M, El-Ghmari A. Intégration des variables spectrales et géomorphométriques dans un SIG pour la cartographie des zones exposées à l'érosion. Revue Télédétection. 2008;**7**:393-404

[11] Maimouni S, Bannari A, El-Hrati A, El-Ghmari A. Potentiels et limites des indices spectraux pour caractériser la dégradation des sols en milieu semi-aride. Journal Canadien de Télédétection. 2012;**37**:285-301. DOI: 10.5589/m11-038

[12] Erskine WD, Saynor MJ. Effects of catastrophic floods on sediment yields in Southeastern Australia. Erosion and sediment yield: Global and regional perspectives. In: Proceedings of the Exeter Symposium, Exeter, UK. July 15–19, 1996. pp. 381-388

[13] SIGMA. Natural catastrophes and man-made disasters in 2014: Convective and winter storms generate most losses. Swiss Re Sigma [Internet]. 2015;**2**(50):1-47. Available from http://www.biztositasiszemle.hu/files/201503/sigma2_2015_en.pdf [Accessed: Mar 18, 2016]

[14] Alexakis DD, Mexis FPK, Vozinaki AEK, Daliakopoulos IN, Tsanis IK. Soil moisture content estimation based on Sentinel-1 and auxiliary earth observation products. A hydrological approach. Sensors. 2017;**17**(6):1455. DOI: 10.3390/s17061455

[15] Wengler L, Weisrock A, Brochier JE, Brugal JP, Fontugne M, Magnin F, et al. Enregistrement fluviatile et paleo-environnements au Pleistocene superieur sur la bordure meridionale

atlantique de l'Anti-Atlas (Oued Assaka, S-O marocain). Quaternaire. 2002;**13**:179-192. DOI: 10.3406/quate.2002.1710

[16] Kerr YH, Waldteufel P, Richaume P, Wigneron JP, Ferrazzoli P, Mahmoodi A, et al. The SMOS soil moisture retrieval algorithm. IEEE Transactions on Geoscience and Remote Sensing. 2012;**50**(5):1384-1403. DOI: 10.1109/TGRS.2012.2184548

[17] Kerr YH, Jacquette E, Al-Bitar A, Cabot F, Mialon A, Richaume P, et al. CATDS SMOS L3 soil moisture retrieval processor algorithm theoretical baseline document (ATBD). Report of CNES and CATDS, France. Reference: SO-TN-CBSA-GS-0029. 2013. 73 p

[18] Bannari A, Teillet PM, Landry R. Comparaison des réflectances des surfaces naturelles dans les bandes spectrales homologues des capteurs TM de Landsat-5 et TME+ de Landsat-7. Revue Télédétection. 2004;**4**:263-275

[19] Wulder MA, White JC, Masek JG, Dwyer J, Roy DP. Continuity of Landsat observations: Short term considerations. Remote Sensing of Environment. 2012;**115**:747-751. DOI: 10.1016/j.rse.2010.11.002

[20] USGS. Shuttle Radar Topography Mission [Internet]. 2008. Available from: http://srtm.usgs.gov/Mission/missionsummary.php [Accessed: Jun 10, 2015]

[21] NASA. Releases Enhanced Shuttle Land Elevation Data [Internet]. 2015. Available from: http://www2.jpl.nasa.gov/srtm/ [Accessed: Jan 10, 2016]

[22] Bannari A, Kadhem G, El-Battay A, Hameid N. Comparison of SRTM-V4.1 and ASTER-V2.1 for accurate topographic attributes and hydrologic indices extraction in flooded areas. Journal of Earth Science and Engineering. 2018;**8**:8-30. DOI: 10.17265/2159-581X/2018.01.002

[23] Maidment RI, Grimes D, Black E, Tarnavsky E, Young M, Greatrex H, et al. A new, long-term daily satellite-based rainfall dataset for operational monitoring in Africa. Scientific Data. 2017;**4**:170063. DOI: 10.1038/sdata.2017.63

[24] NOAA. Climate Prediction Center (CPC) Rainfall Estimator (RFE) for Africa [Internet]. 2015. Available from: https://catalog.data.gov/dataset/climate-prediction-center-cpc--rainfall-estimator-rfe-for-africa [Accessed: Feb 10, 2018]

[25] Lam A, Bierkens MFP, Van-den-Hurk BJJM. Global patterns of relations between soil moisture and rainfall occurrence in ERA-40. Journal of Geophysics Research. 2007;**112**: D17116. DOI: 10.1029/2006JD008222

[26] Wigneron JP, Calvet JC, De-Rosnay P, Kerr YH, Waldteufel P, Saleh K, et al. Soil moisture retrievals from bi-angular L-band passive microwave observations. IEEE Transactions on Geoscience and Remote Sensing. 2004;**1**:277-281. DOI: 10.1109/LGRS.2004.834594

[27] Lievens H, Tomer SK, Al Bitar A, De Lannoy GJM, Drusch M, Dumedah G, et al. SMOS soil moisture assimilation for improved hydrologic simulation in the Murray Darling Basin, Australia. Remote Sensing of Environment. 2015;**168**:146-162. DOI: 10.1016/j.rse.2015.06.025

[28] Myneni RB, Asrar G. Atmospheric effects and spectral vegetation indices. Remote Sensing of Environment. 1994;**17**:390-402. DOI: 10.1016/0034-4257(94)90106-6

[29] Bannari A, Teillet PM, Richardson G. Nécessité de l'étalonnage radiométrique et standardisation des données de télédétection. Canadian Journal of Remote Sensing. 1999; **25**:45-59. DOI: 10.1080/07038992.1999.10855262

[30] Teillet PM, Santer RP. Terrain elevation and sensor altitude dependence in semi-analytical atmospheric code. Canadian Journal of Remote Sensing. 1991;**17**:36-44

[31] Bannari A, Morin D, Bénié GB, Bonn F. A theoretical review of different mathematical models of geometric corrections applied to remote sensing images. Remote Sensing Reviews. 1995; **13**:27-47. DOI: 10.1080/02757259509532295

[32] USGS. Using the USGS Landsat-8 Product [Internet]. 2018. Available from: https://landsat.usgs.gov/using-usgs-landsat-8-product [Accessed: Feb 10, 2018]

[33] Sobrino JA, Jimenez-Muoz JC, Soria G, Romaguera M, Guanter L, Moreno J, et al. Land surface emissivity retrieval from different VNIR and TIR sensors. IEEE Transactions on Geoscience and Remote Sensing. 2008;**46**:316-327. DOI: 10.1109/TGRS.2007.904834

[34] Wigneron JP, Jackson TJ, O'Neill P, De Lannoy G, De Rosnay P, Walker JP, et al. Modelling the passive microwave signature from land surfaces: A review of recent results and application to the L-band SMOS and SMAP soil moisture retrieval algorithms. Remote Sensing of Environment. 2017;**192**:238-262. DOI: 10.1016/j.rse.2017.01.024

[35] Kerr YH, Al-Yaari A, Rodriguez-Fernandez N, Parrens M, Molero B, Leroux D, et al. Overview of SMOS performance in terms of global soil moisture monitoring after six years in operation. Remote Sensing of Environment. 2016;**180**:40-63. DOI: 10.1016/j.rse.2016.02.042

[36] Fernandez-Moran R, Wigneron J-P, De Lannoy G, Lopez-Baeza E, Parrens M, Mialon A, et al. A new calibration of the effective scattering albedo and soil roughness parameters in the SMOS SM retrieval algorithm. International Journal of Applied Earth Observation and Geoinformation. 2017;**62**:27-38

[37] Escorihuela MJ, Chanzy A, Wigneron JP, Kerr YH. Effective soil moisture sampling depth of L-band radiometry: A case study. Remote Sensing of Environment. 2010;**114**(5):995-1001. DOI: 10.1016/j.rse.2009.12.011

[38] Zeng Y, Feng Z, Xiang N. Assessment of soil moisture using Landsat ETM+ temperature/vegetation index in semiarid environment. In: Proceedings of International Geoscience and Remote Sensing Symposium, IGARSS '04; Anchorage, AK, USA. Vol. 6. Sep 20–24, 2004. pp. 4306-4309

[39] Rodrıguez-Fernandez NJ, Aires F, Richaume P, Kerr YH, Prigent C, Kolassa J, et al. Soil moisture retrieval using neural networks: Application to SMOS. IEEE Transactions on Geosciences and Remote Sensing. 2015;**53**(11):5991-6007. DOI: 10.1109/TGRS.2015.2430845

[40] Chen Y, Yang K, Qin J, Cui Q, Lu H, La Z, et al. Evaluation of SMAP, SMOS, and AMSR2 soil moisture retrievals against observations from two networks on the Tibetan Plateau.

Journal of Geophysical Research—Atmosphere. 2017;**122**:5780-5792. DOI: 10.1002/2016JD026388

[41] Tramblay Y, Bouvier C, Martin C, Didon-Lescot JF, Todorovik D, Domergue JM. Assessment of initial soil moisture conditions for event-based rainfall-runoff modelling. Journal of Hydrology. 2010;**387**(3–4):176-187. DOI: 10.1016/j.jhydrol.2010.04.006

[42] Wooldridge SA, Kalma JD, Walker JP. Importance of soil moisture measurements for inferring parameters in hydrologic models of low-yielding ephemeral catchments. Environmental Modelling and Software. 2003;**18**(1):35-48. DOI: 10.1016/S1364-8152(02)00038-5

[43] Aubert D, Loumagne C, Oudin L. Sequential assimilation of soil moisture and streamflow data in a conceptual rainfall-runoff model. Journal of Hydrology. 2003;**280**(1–4):145-161. DOI: 10.1016/S0022-1694(03)00229-4

[44] Massari C, Brocca L, Tarpanelli A, Moramarco T. Data assimilation of satellite soil moisture into rainfall-runoff modelling: A complex recipe? Remote Sensing. 2015;**7**(9):11403-11433. DOI: 10.3390/rs70911403

[45] Cenci L, Laiolo P, Gabellani S, Campo L, Silvestro F, Delogu F, et al. Assimilation of H-SAF soil moisture products for flash flood early warning systems. Case study: Mediterranean catchments. IEEE Journal of Selected Topics in Applied Earth Observation Remote Sensing. 2016;**9**:5634-5646. DOI: 10.1109/JSTARS.2016.2598475

[46] Alvarez-Garreton C, Ryu D, Western AW, Su CH, Crow WT, Robertson DE, et al. Improving operational flood ensemble prediction by the assimilation of satellite soil moisture: Comparison between lumped and semi-distributed schemes. Hydrology and Earth System Sciences. 2015;**19**(4):1659-1676. DOI: 10.5194/hess-19-1659-2015

[47] Brocca L, Ciabatta L, Massari C, Camici S, Tarpanelli A. Soil moisture for hydrological applications: Open questions and new opportunities. Water. 2017;**9**:140. DOI: 10.3390/w9020140